Natural convection in Phase Change Material: Experimental study

Justine Noel, Christel Metivier, Simon Becker, Sebastien Leclerc

To cite this version:

Justine Noel, Christel Metivier, Simon Becker, Sebastien Leclerc. Natural convection in Phase Change Material: Experimental study. International Journal of Heat and Mass Transfer, 2022, 183, pp.122047. 10.1016/j.ijheatmasstransfer.2021.122047 . hal-03388273

HAL Id: hal-03388273
https://hal.univ-lorraine.fr/hal-03388273v1

Submitted on 20 Oct 2021

Natural convection in Phase Change Material: Experimental study

Justine NOEL[a], Christel METIVIER[a,*], Simon BECKER[a], Sébastien LECLERC[a]

[a] *Université de Lorraine, LEMTA, CNRS, NANCY, 54000, FRANCE*

Abstract

Natural convection in a melting material (hexadecane) is studied experimentally using Magnetic Resonance Imaging. This imaging technique allows to discriminate solid and liquid phases and to measure velocity vectors in the volume sample, even through/in opaque phases. Within our experimental conditions, the convection occurs above $Ra \approx 1430$. The thermo-convective flow affects the melting interface leading to higher liquid height in uprising flow and lower liquid height in downward flow regions. Our experiments show that (i) the transient evolution of the mean liquid height $\bar{h}$ is enhanced with convection since $\bar{h} \propto t^{0.8}$ ($\bar{h} \propto t^{\frac{1}{2-3\beta}}$ with $\beta = 1/4$), while $\bar{h} \propto t^{0.5}$ in the conductive regime similarly to the Stefan's problem; (ii) the steady averaged liquid height $\bar{h}$ increases 4 times larger in the convective regime than in the conductive regime. In our experiments the range of A, ratio between the solid and liquid heights, is such as $A > 1.5$. Within this range of values we obtain convective pattern under the form of hexagons / polygons. As the melting boundary grows, we observe a decrease in the polygon number. The polygonal pattern is characterized by a constant dimensionless wavelength, *i.e.* $\lambda/\bar{h} \approx 2$, and thus a constant wavenumber around 3.1 similarly to the primary bifurcation in the classical Rayleigh-Bénard Convection (RBC). Heat transfer is evaluated via the Nusselt number Nu. Close to the onset of convection and above, our results highlight a scaling law $Nu \propto Ra^{\beta}$ with $\beta = 1/4$ similarly to the classical RBC. The kinetic energy E_c is also evaluated via velocity measurements leading to $E_c/E_0 \propto Nu^4$ and therefore to $Re \propto Ra^{2\beta} \propto Ra^{1/2}$. Within the frame of our experiments, all scaling laws are converging to $\beta = 1/4$. They reflect clearly an increase in the convective intensity from both thermal and dynamical points of view.

Keywords: Rayleigh-Bénard convection; Solidification/melting

1. Introduction

Because the issues of energy production, storage and consumption in our societies are nowadays of central importance, the use of Phase Change Materials (PCM) is experiencing a renewed interest. Their interest lies in the phase change occurrence. When the transformation is exothermic (e.g. liquid to solid), the PCM release the heat which is stored during the endothermic transformation (e.g. solid to liquid). In this respect, the latent heat involved during a phase change can be either stored or released. A larger amount of energy - for a small temperature variation - is involved by latent heat than by sensible heat. In a context of energy storage, Phase Change Materials are widely studied since they can be used in a broad range of applications such as heat exchanger technologies, civil engineering, thermal body regulation via the integration of PCM in textiles, food storage during transportation, etc. The numerous applications associated to the PCM give them an outstanding potential. However, their low thermal conductivity does not lead to an efficient rate of heat transfer. For this reason, some studies focus on technological innovations in order to optimize the use of PCM. Without major technological developments, one ‘simple’ way to enhance heat transfer consists in performing the phase change with convection. Moreover, energy storage is not the only domain involving heat transfer and phase change as these mechanisms are widespread in both nature and industry [1]. One example is the melting of ice on Earth, which is of fundamental importance for life on our planet [2, 3, 4]. Furthermore, at these planetary scales, the dynamics of magmatic systems in the Earth crust for instance, is of utmost importance to understand geophysical phenomena. Among the numerous studies on the PCM, we can refer to Stefan’s problems involving both phase change and a dynamical interface. These problems are generally well understood when conduction is the only heat transfer mechanism. Nevertheless, temperature gradients in the melting layer can lead to buoyancy driven flows, *i.e.* convective heat transport in the liquid depth.

Without any phase change, the archetypal configuration involving thermoconvective flows corresponds to a fluid layer heated from below, also called

---

[*]christel.metivier@univ-lorraine.fr

the Rayleigh-Bénard Convection (RBC). Since the experimental study of Bénard [5] and the theoretical one of Lord Rayleigh [6] more than a century ago, the Rayleigh-Bénard configuration has given rise to a large number of studies. For Newtonian fluids, several reviews are proposed in the literature [7, 8, 9].

Beyond the "classical" Rayleigh-Bénard Convection, considering convection with phase change makes the system more complex as the liquid layer evolves in time. In addition to the difficulty of dealing with the coupling between the thermodynamics and hydrodynamics, the stability of a transient system has to be addressed. To avoid this latter difficulty, Busse *et al.* [10]; Davis *et al.*[11] and Dietsche & Müller [12] have considered a steady melting solid heated from below and cooled from above. This configuration can be defined by a steady background state leading to a static equilibrium solution in the conductive regime. Stationary state is obtained provided slow temperature variations at walls. Under these conditions, the stability analysis consists in perturbing a purely conductive liquid layer between two walls, the lower one being a perfect heat conductor. The upper boundary corresponds to the liquid-solid interface maintained at the melting temperature. Because the whole layer is cooled from above, a temperature gradient is induced in the solid layer. In this sense the solid layer can be viewed as an imperfect thermal conductor. Furthermore, the above mentioned studies consider different thermophysical properties in the liquid and solid phases, corresponding to realistic conditions. Within this framework, Davis *et al.* [11] highlight the effective Rayleigh number Ra (based on the liquid height h) and the ratio between the solid and mean liquid heights $A = h_s/\bar{h}$ as the main control parameters. At first order of a weakly non linear analysis, the authors indicate that critical Ra values are obtained between 1493 for $A \geq O(1)$ and the well-known value 1708 when $A = 0$, due to the Ra_c sensitivity with the upper thermal boundary conditions. At larger orders, they study the patterns competition between hexagons and rolls in the frame of small A values, *i.e.* very thin solid phase layer. In the case $A = 0$, rolls are the preferred patterns. For a non zero $A(\ll 1)$ values, the solid phase layer involves an up-down asymmetry in the liquid layer leading to hexagonal patterns characterized by a subcritical bifurcation from the static to the convective solution as also obtained in the classical RBC subject to similar boundary conditions. Increasing Ra, rolls are found stable. There is a range of intermediate Ra values for which hexagons and rolls are both stable. Still increasing Ra, hexagons become unstable and only rolls persist similarly to the classical Rayleigh-Bénard case as studied by Busse [13]. Davis *et al.* [11] and Dietsche *et al.* [12] have proposed an experimental study coupling Rayleigh-Bénard convection and melting/solidification in a single component material. In these papers, local optical observations were possible since the material used, the cyclohexane, is transparent. The frame of their experiments aimed at validating their theoretical results, *i.e.* for quite small A values. Their experimental results allow to obtain the pattern stability diagram on the (Ra, A)-plane. In the range of their experiments, they show that hexagons are obtained for $A > 0.19$ and rolls are obtained when $A < 0.02$. Intermediate values of A correspond to a mixed-patterns region.

A solid phase material maintained at the melting temperature, heated from below leads to an unsteady background state. As underlined by Vasil & Proctor [14], the inherent difficulty when dealing with a melting boundary lies in the feedback between the control parameters (or bifurcation parameter) and the dynamics of the system. In the case of large values of Stefan number St - ratio between the latent heat and sensible heat - Vasil & Proctor [14] obtain separate time scales between the background state (slowly moving interface) and the growth rate of the perturbation. Under this assumption, they develop a perturbation analysis. The linearized analysis leads to a critical Rayleigh number of 1708 for an isothermal liquid-solid interface and an isothermal solid phase considered at the melting temperature. They show that a subcritical morphological instability can occur below the classical convective instability threshold. Indeed, a morphological mode can grow from $Ra = 1296$ and for fixed-flux at the liquid top boundary due to the melting. The weakly nonlinear expansion leads to amplitude equations with time-dependent coefficients. In a recent article, Favier *et al.* [15] do not neither find this threshold value, nor observe any morphological mode in the frame of their computations. According to the authors, this could be related to the numerical processing of the interface or to the very slow melting timescale that is difficult to capture in their simulations. However, Favier *et al.* show that the interface topography can have a strong influence on the onset of convection. Below criticality, a non-planar interface involves the growth of kinetic energy at any value of the effective Rayleigh number. Indeed, non-planar interface can lead to baroclinic flow whatever Ra due to non-aligned pressure gradients and temperature gradients, these latter being normal to the interface [16]. Thus, a small perturbation of the interface destabilizes the conductive base state. If the interface is rendered artificially planar by means of simulations, Favier *et al.* [15] find a critical Rayleigh value around

1710. In any case, when convection occurs, the buoyancy effects involve a distortion of the interface (see Fig. 1) characterized by higher liquid depth in upward fluid regions and reciprocally. The interplay between convection and the topography has led to several studies [17, 18, 19, 20, 21].

Smaller Stefan numbers leading to rapid background state evolution have been investigated numerically by Esfahani *et al.* [22]. The authors show that the smaller St (or the larger the inverse of St as defined in [22]), the more delayed the onset of convection is. We think that this is due to the competition between short melting timescales compared with longer timescales of the thermal diffusivity and convection close to the onset. In their article, Esfahani *et al.* propose also scaling relations for the heat flux, via the Nusselt number.

Theoretical and numerical studies must be completed, or even validated by experiments. The main lock to lead experimental studies comes from the fact that materials are generally opaque in solid phase, making classical optical observations (e.g. Laser Induced Fluorescence LIF, Particle Image Velocimetry PIV) difficult. For this reason, almost all experimental studies concern global measurements such as heat flux at boundaries obtained via thermocouples or InfraRed (IR) thermography. Local temperature measurements are done via thermocouples within the PCM volume [23, 24, 25, 26, 27, 28]. Whenever possible, non-intrusive techniques have to be preferred. Furthermore, a clear understanding of the physical mechanisms at play cannot be achieved without local measurements. From our point of view, the most promising technique to satisfy these criteria is Magnetic Resonance Imaging (MRI). This technique has been used several times in the case of Rayleigh-Bénard Convection without any phase change, see for instance Gibbs *et al.* [29], Weis *et al.* [30], Darbouli *et al.* [31], Skuntz *et al.* [32]. To our knowledge, only Aussillous *et al.* [33] have used this imaging technique in a bidimensional case of a solidifying multi-component PCM layer. Obviously, MRI is involved in many studies related to medicine. However, in the fields of physics or engineering, this tool is less widespread. It allows to image through opaque systems, to measure velocity vectors in liquid phases, to differentiate solid and liquid phases and even to measure temperature fields [34]. Finally, few experimental studies have been proposed: only Davis *et al.* [11] and Dietsche *et al.* [12] brought some experimental results validating their theoretical stability analyses (critical conditions and pattern selection) in the frame of a steady background state and small A values, that is to say thin solid phase above the liquid layer. Only one material was involved in these studies and their results have never been compared to other (independent) experiments. Furthermore, there is still a lack of experimental investigations since some recent theoretical and computational studies have never been validated even close to the onset of convection [14, 15]. In this respect, the present work intends to investigate experimentally the Rayleigh-Bénard convection with a melting boundary. We aim at validating the former studies as well as providing new experimental results to highlight the interplay between convection and phase change. We focus on the melting of a single-component material, hexadecane, heated from below and cooled from top for both unsteady and steady melting background states. In this paper we also extend experiments to larger A values, since we melt a bulk solid phase leading to a range of A between infinity to the order of 1. As explained in the following section "Materials and methods", the studied configuration allows us to investigate both the unsteady melting case by imposing a large temperature difference to the initially isothermal solid as well as the steady case similarly to Davis *et al.* [11]. By using MRI, we propose to investigate the onset of convection, its influence on the liquid height evolution and on the flow features. A particular interest is also dedicated to heat transfer as well as the increase in the convection intensity through the kinetic energy. Our results obtained in unsteady and steady configurations are presented in section 3. Finally, our work ends with concluding remarks.

2. Materials and methods

2.1. Material properties

The Phase Change Material studied is 99% pure hexadecane, an organic PCM supplied by Sigma Aldrich (CAS Number 544-76-3, ref. H6703). This material presents some well known thermal properties as given by Velez *et al.* [35]. We have checked and completed its thermodynamic and physical properties [36]. The relevant properties for this present paper are summarized in Table 1. Thermal properties obtained in our framework are in a very good agreement with that ones given by Velez *et al.* [35].

Hexadecane is characterized by a Stefan number St given as follows:

$$St = \frac{\Delta H_f}{c_p \Delta T} \approx 110 \tag{1}$$

with a temperature difference of $\Delta T = 1$°C. The quite large value in St reflects clearly a much larger heat transfer by latent heat compared with sensible heat. In the liquid phase, the Prandtl number is estimated around $T = 20\,$°C:

$$Pr = \frac{\nu}{\kappa} = 45. \tag{2}$$

with $\nu = \eta/\rho$ the kinematic viscosity and $\kappa = \Lambda/(\rho c_p)$ the thermal diffusivity.

2.2. Experimental device and protocols

The experimental device consists of a cylindrical cavity of diameter D and height H. Two aspect ratios $AR = D/H$ have been investigated in our experiments: AR=5.9 (H = 20 mm, D = 118 mm) and AR=4.56 (H = 25 mm, D = 114 mm). The PCM is placed between two horizontal 3.1 mm thick plates made of sapphire, characterized by a thermal conductivity $\Lambda_{sapphire} = 35-40$ W m^{-1} K^{-1}. Such thin plates and large thermal conductivity lead to a negligible temperature variation within the plates thickness. The temperatures at these surfaces are imposed by temperature controlled water baths leading to a temperature at the upper wall T_u and a temperature at the bottom wall T_d (indices 'u' and 'd' are used for up and down respectively). Thermocouples (type K) are placed at the inlet and outlet water flows outside the MRI resonator in order to not perturb MRI measurements. All materials of the setup are non-metallic to avoid perturbations of the spectrometer magnetic field. The cylinder side is made of polymethyl methacrylate (PMMA). An insulating foam is added around the lateral wall during experiments. A schematic representation of the device is shown in Fig. 2. The whole device is placed in a temperature controlled room at 24 °C.

Initially the volume sample is maintained at a homogeneous cold temperature T_c such as $T_u = T_d = T_c < T_m$, in order to have the whole PCM layer in solid state. Then, one of the two walls is heated in order to obtain a partial melting of the PCM sample. Two configurations are employed in this study: 1) $T_u > T_d = T_c$, *i.e.* the PCM layer is heated from above, to investigate the stable conductive regime; 2) $T_u = T_c < T_d$ (heated from below) which corresponds to the unstable configuration. In this case, we change the temperature difference $\Delta T = T_d - T_u > 0$ by imposing several increments in order to increase the liquid height. The waiting time is 14 hours between each increment. The unsteady background state, *i.e.* a time-dependent PCM melting, has been investigating by imposing one large ΔT to the material in solid phase. Results are presented in section 3.1.

Similarly to Davis *et al.* [11], the steady melting state has been investigated by slowly varying ΔT by 0.5 ° C steps lasting at least 12 hours. In the case where $\Delta T > 0$, two protocols have been carried out: (1) $T_u = T_c$ is fixed and the lower wall is gradually heated leading to an increasing ΔT and (2) the upper cold temperature is gradually increased only leading to a decrease in ΔT (T_d fixed) and an increase in the liquid height. This latter protocol has the advantage to keep constant the temperature difference through the liquid phase. In this sense, the liquid height h is the only varying parameter regarding the Rayleigh number in the liquid phase. Experimental runs last typically about 2 to 4 weeks in order to ensure steady states are obtained. Results are presented in section 3.2.

2.3. MRI Protocols

Local measurements of velocity are obtained using Magnetic Resonance Imaging (MRI). Velocity vectors can be obtained locally (at each voxel) in the three space directions. Measurements can be done in the whole PCM volume. However, for time constraints reasons, we choose two relevant planes to measure velocities: one horizontal plane – parallel to the (XY) plane (Figure 1) - preferably located in the center of the liquid layer and one vertical plane - the (XZ) plane - which contains the axis of the cylindrical cavity. Furthermore, the location of the liquid and solid phases can be obtained at each voxel. Indeed, MRI allows to discriminate liquid and solid phases as the latter does not give any signal. The measurements are carried out in the same planes as those used for velocity measurements.

Magnetic Resonance Imaging experiments are carried out on a Bruker Avance Biospec 24/40 spectrometer equipped with a 200 mm inner diameter gradient coil and 160 mm diameter quadrature resonator. This magnetic field is 2.34 T and the proton resonance frequency of 100.3 MHz. We use RARE (Rapid Acquisition with Relaxation Enhancement) experiments [37] to acquire fast proton density map with transverse relaxation time weighting in order to distinguish liquid and solid phases. As said previously, the solid phase does not give any signal due to its very fast transverse relaxation time [38]. These RARE experiments are of great importance as we can determine the melting evolution of the material. Moreover, an accurate knowledge of the liquid height is crucial to evaluate the Rayleigh number in the liquid phase. For this purpose, we work with a pixel resolution of 100 μm in the vertical (Z) direction.

Velocity vectors are acquired using a spin-echo protocol with additional flow encoding gradient pulses, the sequence is represented in Fig. 3. The gradient pulses duration (δ) is 4ms and the gradient separation time (Δ) is 12 ms. The repetition time is 1000 ms and the echo time is 28 ms.

The signal phase ϕ is:

$$\phi = \gamma G \delta \Delta v \tag{3}$$

with γ is the gyromagnetic ratio of proton ($\gamma = 2.675\ 10^8$ rad T^{-1} s^{-1}), G is the flow encoding gradient pulses intensity and v the component of velocity in the direction of the applied gradient. The accuracy of velocity measurements is 5.10^{-5} m s^{-1} according to previous works with the same parameters [31]. To obtain a map of one velocity component, we acquire two images with two G values (typically 180 mT/m and 0 mT/m, but it can be adjusted according to the velocity amplitudes). The difference between these two images leads to one velocity component. The other velocity components are obtained in the same way.

3. Results

3.1. Unsteady background state

In this section, we investigate the influence of the Rayleigh-Bénard convection with an upper moving interface (melting interface). Initially, the material is subjected to isothermal conditions ($T_d = T_u = 10.5^\circ$ C) at the upper and lower walls so that the whole sample is in the solid phase. This initial step lasts about 12 hours. After ensuring with MRI measurements that the bulk material is solid, a temperature difference $\Delta T = T_d - T_u = 9.6^\circ$ C is applied to the layer such that the lower wall temperature is above the melting point $T_m < T_d = 20.1\,^\circ$C. The melting time evolution is depicted in Movie 1 (supplementary materials) in which images correspond to protons density measurements (RARE experiments) in a vertical plane at the center of the cavity. These measurements allow to differentiate the solid phase (grey regions) and the liquid phase (white regions). As expected, the melting starts at the bottom wall and propagates in the upward vertical direction with time, leading to a liquid layer growing from below. Since the Stefan number is high, the melting time scale is slow qualifying the unsteady background state to nearly successive quasi-steady states. As long as the solid-liquid interface remains horizontal and homogeneous throughout the volume, the regime remains conductive, no significant velocity values are measured in the frame of our experimental resolution (Fig. 4 (a)). Convection occurs when the liquid depth, therefore the effective Rayleigh number Ra, is large enough. The effective Rayleigh number based on the mean liquid height $\bar{h}$ is defined by:

$$Ra = \frac{\rho g \alpha (T_d - T_m) \bar{h}^3}{\eta \kappa} \tag{4}$$

where g is the gravity.

The onset of convection is characterized by a distortion of the interface coupled with an increase in velocity values as represented in Fig. 4 (b). As expected, positive velocity values of V_Z (upward flow) lead to increase locally the liquid height. Reciprocally, negative V_Z values are accompanied by a decrease in the liquid height. This is the result of temperature variations in the cavity in which hotter (resp. colder) zones correspond to upward (resp. downward) flow regions. We have evaluated the local Rayleigh number - Ra based on the local liquid height h - in order to determine a value above which convection is obtained. Local Ra values (crosses) are displayed in Fig. 5, the liquid height is also represented (blue symbols). In this figure, dotted lines correspond to critical values of Ra obtained in the case of (1) an unsteady melting boundary Vasil & Proctor [14] $Ra = 1296$, (2) a steady background state Davis *et al.* [11] leading to critical Ra varying from $Ra = 1493$ for $A > 1$ (3) to $Ra = 1708$ for $A = 0$, *i.e.* the classical RBC. As a remark, we could underline that (2) and (3) correspond to the RBC for which boundary conditions vary with A. As summarized in Table 2, our results (presented in Figs. 4-6) are obtained for $A > 1.9$. It means that the solid height is always larger than the liquid one involving a significant asymmetry in up-down thermal boundary conditions: the upper one corresponds to a low conductor of a mean thickness $H - \bar{h}$. From our velocity amplitudes (greater than 5.10^{-5} m/s) in the liquid phase, we observe that convection has invaded the entire liquid layer (Fig. 4 (b)). In particular, we observe that convection occurs above $Ra \approx 1430$, which is the minimal local Rayleigh number. At the onset of convection, the melting rate is such as $A = 5.4$. This set of values (Ra, A) is in agreement with the one proposed by Davis *et al.* [11], that is to say $Ra_c = 1493$. Furthermore, Vasil & Proctor [14] do not consider conduction in the upper solid phase, in which perturbations can grow. This latter point should explain the difference with our experimental results.

Convective patterns as well as typical wavelength and wavenumber can be obtained by considering the vertical velocity component in a horizontal cross-section as represented in Fig. 6. In the light of these results, we observe polygonal patterns, *i.e.* hexagonal patterns whose defects increase with decreasing effective aspect ratio $D/\bar{h}$ in the liquid layer. In other words, well formed hexagons or mixed polygonal patterns are observed similarly to numerical results provided by Esfahani *et al.* [22]. As above mentioned, obtaining hexagonal patterns is not surprising since they result from a vertical asymmetry: the up and down boundary conditions of the liquid layer are different. The lower wall is a good thermal conductor and the upper interface is considered as an imperfect thermal conductor. This vertical asymmetry is enhanced with the surface deflection. Within the assumption of small A values, Davis *et al.* [11] obtained hexagons for $A > 0.19$. In our experiments, the range of A values is widespread $A > 1$. We can conclude that theoretical results [11] remain valid for large values of A. Figure 6 shows that the hexagons wavelength increases coupled with a decreasing number of cells when the effective aspect ratio in the fluid layer $D/\bar{h}$ decreases. This is quantified in Fig. 7 which displays histograms of the dimensionless wavelengths $\lambda/\bar{h}$ normalized by the probability density function pdf, where λ is the length between the polygon centers (local maxima of the velocity V_Z) and the neighbouring polygon centers.The most frequent dimensionless wavelength obtained is $\lambda/\bar{h} \approx 2$, corresponding to a wavenumber about 3.1. As the liquid height increases, polygons merge leading to bigger ones. In Figure 7, the continuous line corresponds to the normal distribution f defined by:

$$f(\lambda/\bar{h}) = \frac{1}{\sigma\sqrt{2\pi}} e^{-\frac{1}{2}\left(\frac{\lambda/\bar{h}-\mu}{\sigma}\right)^2} \tag{5}$$

where μ and σ^2 correspond to the mean and variance. μ is obtained around 2 for all frames, *i.e.* at different times and liquid heights. Due to solid areas that are too large, we have not considered the case represented by Fig. 6 (b). We observe that the histograms in Fig. 7 present small differences while the liquid layer increases. The scatter in wavelength highlights that patterns correspond to mixed polygons rather than regular hexagons.

These results are in good agreement with the numerical studies provided by Esfahani *et al.* [22], Madruga and co-workers [18, 27]. In these latter articles, the authors investigate by numerical means the dynamics of thermal plumes during the melting of a PCM. They observe four different regimes: (1) the conductive, (2) the linear, (3) the coarsening and (4) the turbulent regimes. The second regime is the destabilization of the conductive regime through a linear Rayleigh-Bénard instability. This regime is characterized by a constant wave number determined by the primary Rayleigh-Bénard instability. The third regime, that Madruga & Curbelo [18] observe numerically, corresponds to the development of a secondary instability which leads to the merge of cells as the liquid height increases and a coarsening of thermal plumes. This regime is such that the convective patterns conserve a roughly constant wave number (similar to that one obtains at the onset of Rayleigh-Bénard convection). The authors highlight the possible development of a horizontal mode with a finite wavenumber during the coarsening of the plumes and the merge of cells. An obvious consequence is the decreasing number of cells and an increasing wavelength as obtained in our experiments. Furthermore, for increasing Ra, Madruga & Curbelo obtain a more erratic motion characterized by a range of different plumes scales. It explains why the authors obtain smaller distorsions of the melting interface with increasing time and Ra.

As time advances, we observe an increase in the liquid height as well as an increase in the convection intensity since velocity amplitudes increase until the steady state is reached. Figure 8 represents the dimensionless averaged liquid height $\bar{h}/H$ throughout a dimensionless time, the Fourier number Fo defined as follows:

$$Fo = t\frac{\kappa}{H^2}$$

Results obtained in the convective regime ($\Delta T = 9.6\,°\mathrm{C}$ and $\Delta T = 5.5°\mathrm{C}$, Fig. 8 (b)) are compared with the ones obtained in a stable conductive regime ($\Delta T = -7.2\,°\mathrm{C}$ and $\Delta T = -6.6\,°\mathrm{C}$ Fig. 8 (a)). The stable conductive configuration is close to the Stefan's problem [39] for which the material is initially in solid phase at the melting temperature. The application of a temperature larger than T_m at one boundary (the other one being insulated) leads to the melting of the material, its propagation being in the normal direction to the boundary. It is found that in a semi-infinite domain, the liquid height increases as $h \propto t^{0.5}$. We have extended this study to our configuration, *i.e.* a finite domain with independent isothermal conditions at each horizontal wall (details are provided in Appendix 2). Our numerical computations are displayed in Fig. 8 (a) by continuous lines; they are in very good agreement with our experimental results (small crosses). We recover in the conductive regime a similar scaling law given by $h \sim \sqrt{D_{eff} \times t}$, D_{eff}

being an effective thermal diffusion coefficient.

When convection occurs, the melting is enhanced since $\bar{h}$ grows more rapidly in time as can be observed in Fig. 8 (b). At the very beginning of the experiments (yellow and pink), our results fit well with continuous lines (obtained by computations in the conductive regime). Then, our results start to increase more rapidly deviating from the conductive regime. The inset in Fig. 8 (b) focuses on the unsteady evolution of the liquid height when convection arises. From an energetic argument, Favier *et al.* show that considering the usual scaling law $Nu \propto Ra^{\beta}$, one obtains $\bar{h} \propto t^{1/(2-3\beta)}$ for fixed Pr. The range values of our experimental parameters, *i.e.* quite low Ra and $Pr \approx 45$, places our study in the regime for which $\beta = 1/4$ as defined by Grossmann *et al.* [40] who considered the classical Rayleigh-Bénard convection. With $\beta = 1/4$, we obtain $\bar{h} \propto t^{0.8}$ which corresponds precisely to the best fit for our experimental results (see the continuous black lines in the inset of Fig. 8 (b)).

In the unsteady case, the heat transfer $\phi_{t/l}$ provided to the liquid phase at the solid-liquid interface can be evaluated by the sum of the conductive heat flux through the solid and the enthalpy due to the phase change process:

$$\phi_{t/l} = \Lambda_s \frac{T_m - T_u}{H - \bar{h}} + \rho \Delta H_f \frac{\partial \bar{h}}{\partial t} \tag{6}$$

In this case, the Nusselt number - ratio between the total heat $\phi_{\mathrm{t/l}}$ through the liquid and the heat $\phi_{\mathrm{cond/l}}$ due to conduction in the liquid height - is given by:

$$Nu = \frac{\phi_{\mathrm{t/l}}}{\phi_{\mathrm{cond/l}}} = \frac{\Lambda_s}{\Lambda_l} \frac{\bar{h}}{H - \bar{h}} \frac{T_m - T_u}{T_d - T_m} + \frac{1}{\Lambda_l} \frac{1}{T_d - T_m} \rho \Delta H_f \bar{h} \frac{\partial \bar{h}}{\partial t} \tag{7}$$

$$\begin{aligned} Nu &= \frac{\Lambda_s}{\Lambda_l} \frac{\bar{h}^*}{1 - \bar{h}^*} \frac{\theta}{1 - \theta} + St\, \bar{h}^* \frac{\partial \bar{h}^*}{\partial t^*} && (8) \\ &= \frac{\Lambda_s}{\Lambda_l} \frac{\bar{h}^*}{1 - \bar{h}^*} \frac{\theta}{1 - \theta} + \frac{St}{2} \frac{\partial \left(\bar{h}^*\right)^2}{\partial t^*}. && (9) \end{aligned}$$

with $\phi_{\mathrm{cond/l}} = \dfrac{\Lambda_l}{\bar{h}}(T_d - T_m)$, $St = \dfrac{\Delta H_f}{c_p(T_d - T_m)}$, $\bar{h}^* = \dfrac{\bar{h}}{H}$ and $t^* = Fo$. In Equation (9), we have also introduced the parameter θ defined by:

$$\theta = \frac{\Delta T_{solid}}{\Delta T_{total}} = \frac{T_m - T_u}{T_d - T_u} \tag{10}$$

As a first approximation, the Nusselt number is calculated considering the mean liquid height $\bar{h}^*$ (Fig. 9). More accurate values can be obtained considering local liquid height [15]. Considering the scaling law for $\bar{h}^*$ with time, whose dimensionless form writes $\bar{h}^* \propto Fo^{0.8}$, the Nusselt becomes:

$$Nu \propto \left(a \times \frac{\theta}{1-\theta}\right) \frac{Fo^{0.8}}{1 - Fo^{0.8}} + St \times 0.8 \times Fo^{0.6}$$

where a is the conductivity ratio, $a = \Lambda_s/\Lambda_l$. At the very beginning of the convection, *i.e.* $Fo \ll 1$, we can write:

$$Nu \propto \left(a \times \frac{\theta}{1-\theta}\right) Fo^{0.8} + St \times 0.8 \times Fo^{0.6}$$

In this asymptotic region, the part due to the phase change plays a major role. Heat transfer depends on the Stefan number, St, in transient regimes. By waiting long time enough, the average height reaches a stationary value, leading to the following expression for the Nusselt number:

$$Nu = \left(a \times \frac{\theta}{1-\theta}\right) \frac{\bar{h}^*}{1 - \bar{h}^*}. \tag{11}$$

3.2. Steady background state

As mentioned above, we have also investigated steady states by varying slowly the temperature difference between the horizontal walls. For that purpose, we wait about 12-14 hours after each small ΔT increment. We have verified at each temperature step that the waiting time was larger than the time needed to obtain a steady mean height value, it is reached around 7 hours in the convective regime and less in the conductive regime. It turns out that in the frame of our experiments, both $\bar{h}$ and patterns reach a stationary regime.

The steady dimensionless mean liquid height $\bar{h}^*$ is depicted in Fig. 10 as a function of the theoretical value obtained in the steady conductive regime (see Appendix 1 for details):

$$h^*_{cond} = \left(\frac{h}{H}\right)_{cond} = \frac{1-\theta}{1-\theta+\frac{\Lambda_s}{\Lambda_l}\theta} \tag{12}$$

Note that in the steady conductive regime, we have $\bar{h} = h$ since the interface is planar.

In Figure 10, the crosses correspond to our experimental results in the case of stable heat-conduction regime ($\Delta T < 0$). The continuous line corresponds to the theoretical results for this regime, *i.e.* the first bisector. This configuration highlights a good agreement between our experiments and the theory. The circles represent the unstable configuration where $\Delta T > 0$. For small ΔT values or small liquid height, the unstable conductive solution is observed (full circles) and fits well the theory. The convective regime occurs for larger heights of the liquid layer (empty symbols). We observe a significant change in slope when convection occurs. The dimensionless liquid height increases 4 times larger than the one obtained in the conductive regime as highlighted by the slope of dashed lines. It means that the convective regime enhances significantly the PCM melting. This is because convection improves heat transfer as observed in Fig. 11 which displays the Nusselt number Nu as a function of Ra. At steady states, there is no longer any phase change, meaning that heat transfer from the solid phase balances that of the liquid phase, leading to the Eq. (11) for Nu.

In addition to the transient increase in the liquid height, the proposed value for $\beta(= 1/4)$ lies also for further scaling laws in the convective regime such as $Nu \sim Ra^{\beta}$ even for moderate Ra values. Within our experiments, we recover this trend as highlighting in Fig. 11. It also highlights the significant increase in Nu values above the onset of convection within the range $Ra_c \leq \; Ra \leq O(10^5)$. This result is in good agreement with the literature. As already discussed in the previous section, the range of our control parameters, *i.e.* moderate Ra values and $Pr \approx 45$, is within Regime I, as defined by Grossmann & Lohse [40] and Stevens *et al.* [41] in the classical Rayleigh-Bénard Convection (RBC). In this regime, the kinetic and thermal boundary layers are thick and they correspond to dominant contributions in terms of dissipation rates. They also propose the following scaling law

$$Re \sim Ra^{2\beta},$$

where the Reynolds number is $Re = (UH)/\nu$, with U the mean large-scale velocity corresponding to the convective cell velocity. In their article, Grossmann & Lohse show that $\beta = 1/3$ is obtained in the regime IV_u which corresponds to larger Ra and Pr values and to dominant contributions of the bulk in terms of viscous and thermal dissipation rates as defined in [40]. In the case of Rayleigh-Bénard Convection with a melting interface, Esfahani *et al.* [22] as well as Favier *et al.* [15] found, by numerical means, $\beta = 1/3$ but (as said by the authors) smaller values such as 1/4 can also be possible.

It is worth interesting to focus on the dynamics within the liquid layer. As could be expected, the increase in heat transfer is accompanied by an increase in convection intensity, visible not only through the velocity amplitudes but also through the mean kinetic energy. The mean kinetic energy E_c is evaluated from velocity measurements in the vertical plane (X, Z), it is defined as follows:

$$E_c = \frac{1}{2}\rho\frac{1}{\mathcal{S}}\int_{\mathcal{S}}(V_X^2 + V_Y^2 + V_Z^2)d\mathcal{S} \tag{13}$$

where $\mathcal{S}$ represents the surface area of liquid phase in the plane (X, Z). We consider the dimensionless kinetic energy E_c/E_0, where

$$E_0 = \frac{1}{2}\rho g\alpha(T_d - T_u)H \tag{14}$$

is a characteristic kinetic energy based on the potential thermal energy in the entire layer of height H.

Figure 12 presents kinetic energy as a function of the Nusselt number. Results reflect the following scaling law:

$$\frac{E_c}{E_0} \sim Nu^4.$$

Since $Nu \sim Ra^{1/4}$ and $E_c \sim U^2$, it leads to $Re \sim U \sim Ra^{1/2}$. Our results follow similar scaling laws as proposed in the regime I for the classical RBC, *i.e.* $\beta = 1/4$.

Concerning the convective patterns obtained in steady states, they are depicted in Fig. 13 for different temperature steps and cavity heights ($H =$ 0.02 m and $H = 0.025$ m). In the frame of our experiments, *i.e.* for an effective aspect ratio such that $D/\bar{h} \geq 10$, we also observe polygons with a dimensionless wavelength $\lambda/\bar{h} \approx 2$ similarly to that ones obtained during transient states. As already mentioned, characteristic time of the hexadecane melting is quite large leading to consider transient states as quasi-steady states (similarly to the framework of Vasil & Proctor [14]). That can explain why transient background state tends to the steady ones. As a consequence, it is not surprising to observe (imperfect) polygons since our experimental conditions are such as $A > 0.9$. Our results are summarized in the (Ra, A)-plane in Fig. 14, results from previous work [11] are added. Our experimental results allow to show that the theoretical work of Davis *et al.* [11] is still valid to larger values of A since we observe (imperfect) polygons in the region $A > 0.9$. The larger is A, the stronger is the up-down asymmetry and polygons are still the preferred convective pattern. We observe that the primary bifurcation is stabilized by the topology since a constant wavenumber as well as the polygonal pattern are conserved even for large Ra values.

4. Conclusion

The Rayleigh-Bénard Convection in a melting material, the hexadecane, is studied experimentally using the Magnetic Resonance Imaging. The hexadecane, a linear alcane, corresponds to a pure (mono-component) material. It is characterized by a single value for the melting/freezing temperature as well as a large Stefan number $St = 110$ and $Pr = 45$. The melting of a solid material in the conductive regime results in a planar solid-liquid interface parallel to the heated wall. When the material is heated from below, the motionless conductive regime can be destabilized in the liquid phase, leading to the onset of convection. The thermo-convective flow is characterized by motion in the liquid layer which affects the melting interface. Regions of uprising fluid (hot) increase locally the liquid height, reciprocally regions of descending fluid (cold) decrease locally the liquid height.

Within our experimental conditions, such as $A > 0.9$, convection occurs above a critical Rayleigh number of $Ra_c \approx 1430$ and the convective pattern corresponds to (imperfect) hexagons for both unsteady and steady background melting states. Our experimental results confirm that ones proposed by Davis *et al.* [11] in the case of a steady background state. Whether the motionless liquid layer is steady, the classical Rayleigh-Bénard case - for which the lower wall is a perfect conductor and the upper one is an imperfect conductor - leads to $Ra_c = 1493$ and hexagonal convective patterns when developing a perturbation analysis for small A values as done by Davis *et al.* [11]. However, different critical conditions were obtained either theoretically or numerically in the case of an unsteady melting boundary [14, 15], due to different boundary conditions. Original results in terms of convective patterns are provided in the present paper for quite large values of A. As the mean liquid height increases, we observe that hexagons become more imperfect which could be attributed to wall effects since the effective aspect ratio decreases. This is also attributed to a decrease in the polygon number as the melting boundary is growing. It means that some polygons merge as the liquid height increases. This is characterized by a constant dimensionless wavelength, *i.e.* $\lambda/\bar{h} \approx 2$, and thus a constant wavenumber about 3.1 similarly to the primary bifurcation in the classical Rayleigh-Bénard Convection.

Our experiments show that (i) the transient evolution of the liquid height is enhanced with convection since $\bar{h} \propto t^{\frac{1}{2-3\beta}}$ with $\beta = 1/4$, while $\bar{h} \propto t^{1/2}$ in the conductive regime ; (ii) the steady averaged liquid height $\bar{h}$ is increased by a factor 4 in the convective regime compared with the conductive regime. In transient convective regime, the Stefan number plays a significant role in the heat transfer. In steady convective regimes, our results highlight scaling laws $Nu \propto Ra^{\beta}$ similarly to the classical RBC. Furthermore, our velocity measurements allow to evaluate the kinetic energy leading to $E_c/E_0 \propto Nu^4 \propto Ra^{4\beta}$ with $\beta = 1/4$. These results reflect an increase in the convective intensity from both thermal and dynamical points of view.

Finally, this present paper provides a complete experimental study dealing with the phase change of a pure material in convective regime. Important and additional findings are achieved from our experiments in regard to available results in the literature. The resulting conclusions can be extended to a wide range of single-component PCMs. For the future, we intend to investigate the onset of convection for smaller values of A as well as investigate the convection for still larger Ra. We would also vary boundary conditions and/or other materials in order to investigate the influence of control parameters, e.g. A, Ra, St, Pr, on the coupling between transient melting boundary, convection and heat transfer. Multi-component materials will also be studied. Obtaining temperature fields in addition to velocity vectors and phases is our next goal in order to understand more deeply physical mechanisms at play during the phase change.

Acknowledgements

Financial supports have been brought to this work by the operation "STOCK'NRJ" co-financed by the European Union within the framework of the Program FEDER-FSE Lorraine and Massif des Vosges 2014-2020.

The authors greatly acknowledge the "Plateforme de RMN de l'Institut Jean Barriol, Université de Lorraine".

Appendix 1 - Steady conductive regime

At steady conductive regime, heat flux at the solid-liquid interface is only due to conduction in liquid ϕ_l and solid ϕ_s phases. Then, we write:

$$\phi_s = \phi_l$$

with

$$\phi_l = \frac{\Lambda_l (T_d - T_m)}{\bar{h}} \quad \text{and} \quad \phi_s = \frac{\Lambda_s (T_m - T_u)}{H - \bar{h}}.$$

Then, we write:

$$\frac{\Lambda_l (T_d - T_m)}{\bar{h}} = \frac{\Lambda_s (T_m - T_u)}{H - \bar{h}}$$

Introducing θ as defined by Eq. (10), it follows:

$$\frac{\bar{h}}{H - \bar{h}} = \frac{\Lambda_l}{\Lambda_s} \left(\frac{T_d - T_u}{T_m - T_u} + \frac{T_u - T_m}{T_m - T_u} \right) = \frac{\Lambda_l}{\Lambda_s} \left(\frac{1}{\theta} - 1 \right)$$

After some algebra, we finally obtain Eq. (12):

$$\frac{\bar{h}}{H} = \frac{1 - \theta}{\frac{\Lambda_s}{\Lambda_l} \theta + 1 - \theta}$$

Appendix 2 - Simulation of the phase change in conductive regime

In this appendix, we detail the modelisation of a melting solid between two paralell walls in the conductive regime as represented in Fig. 1 (upper part "Conduction"). The interface is noted $I(t)$. The governing equations are:

$$\frac{\partial^2 T_l}{\partial z^2} = \frac{1}{\kappa_l}\frac{\partial T_l}{\partial t} \qquad z < I(t) \tag{15}$$

$$\Lambda_s \frac{\partial T_s}{\partial z} - \Lambda_l \frac{\partial T_l}{\partial z} = \rho \Delta H_f \frac{dI}{dt} \qquad z = I(t) \tag{16}$$

$$\frac{\partial^2 T_s}{\partial z^2} = \frac{1}{\kappa_s}\frac{\partial T_s}{\partial t} \qquad z > I(t) \tag{17}$$

assorted by the following initial condition

$$T(t=0,z) = T_{ini} \tag{18}$$

and by the boundary conditions

$$T(t, z = I(t)) = T_m \tag{19}$$

$$T(t, z = 0) = T_d \tag{20}$$

$$T(t, z = H) = T_u \tag{21}$$

We set

$$\text{Dimensionless temperature } \Theta = \frac{T - T_{ini}}{T_m - T_{ini}} \tag{22}$$

$$\text{Dimensionless time } t^* = t \times \frac{\kappa_l}{H^2} \tag{23}$$

$$\text{Dimensionless space } z^* = \frac{z}{H} \tag{24}$$

We note a the ratio of the conductivities $a = \Lambda_s/\Lambda_l$. The dimensionless form of Eqs. (15),(16),(17) are:

$$\frac{\partial^2 \Theta_l}{\partial z^{*2}} = \frac{\partial \Theta_l}{\partial t^*} \qquad z^* < I^*(t) \tag{25}$$

$$\frac{\partial \Theta_l}{\partial z^*} - a\frac{\partial \Theta_s}{\partial z^*} = St\frac{dI^*}{dt^*} \qquad z^* = I^*(t) \tag{26}$$

$$\frac{\partial^2 \Theta_s}{\partial z^{*2}} = \frac{1}{a}\frac{\partial \Theta_s}{\partial t^*} \qquad x^* > I^*(t) \tag{27}$$

assorted by the dimensionless initial and boundary conditions:

$$\Theta_l(t^* = 0, z^*) = \Theta_s(t^* = 0, z^*) = 0 \tag{28}$$

$$\Theta(t^*, z^* = I^*(t^*)) = 1 \tag{29}$$

$$\Theta_l(t^*, z^* = 0) = \Theta_d = \frac{T_d - T_{ini}}{T_m - T_{ini}} \tag{30}$$

$$\Theta_s(t^*, z^* = 1) = \Theta_u = \frac{T_u - T_{ini}}{T_m - T_{ini}} \tag{31}$$

This set of equations (25)-(28) is discretized by using the finite difference method. The interface is located at $i+1$, the wall $z=0$ is located at $i=1$ and the wall $z=H$ is located at $i=N$. In the liquid phase, Eq. (25) becomes:

$$\frac{\Theta^{n+1}_{l,i+1} - 2\Theta^{n+1}_{l,i} + \Theta^{n+1}_{l,i-1}}{\Delta z^2} = \frac{\Theta^{n+1}_{l,i} - \Theta^{n}_{l,i}}{\Delta t_n}$$

$$\Theta^{n}_{l,i} = -r_n\Theta^{n+1}_{l,i+1} + (1+2r_n)\Theta^{n+1}_{1,i} - r_n\Theta^{n+1}_{l,i-1} \tag{32}$$

with $r_n = \dfrac{\Delta t_n}{\Delta z^2}$.

Similarly in the solid phase, Eq. (27) becomes:

$$\Theta^{n}_{s,i} = -ar_n\Theta^{n+1}_{s,i+1} + (1+2ar_n)\Theta^{n+1}_{s,i} - r_n\Theta^{n+1}_{s,i-1} \tag{33}$$

The interface equation (26) allows us to deduce the time step Δt_n during which the interface moves with a distance Δz.

$$\Delta t_n = \Delta z^2 \times St\left(\Theta^{n+1}_{l,i+1} - \Theta^{n+1}_{l,i} - a\Theta^{n+1}_{s,i+2} + a\Theta^{n+1}_{s,i+1}\right)^{-1} \tag{34}$$

Since at the interface, $\Theta^{n+1}_{l,i+1} = \Theta^{n+1}_{s,i+1} = \Theta_m = 1$, we deduce

$$\Delta t_n = \Delta z^2 \times St\left((1+a)\Theta_m - \Theta^{n+1}_{l,i} - a\Theta^{n+1}_{s,i+2}\right)^{-1} \tag{35}$$

At $t^* = 0$ ($n = 0$), we set that the interface is at $i+1 = 2$, then $\Theta^{n+1}_{s,i+2} = 0$ and $\Theta^{n+1}_{l,i} = \Theta_d$ according to Eqs. (28) and (30). The initial time step is :

$$\Delta t_0 = \frac{\Delta z^2 \times St}{(1+a)\Theta_m - \Theta_d} \tag{36}$$

Finally, the system to solve is summarized below under matrices form. In the liquid phase, we write $AK^{n+1} = K^n + C$ corresponding to

$$\begin{bmatrix} 1 & 0 & \cdots & \cdots & 0 \\ -r_n & 1+2r_n & -r_n & 0 & \cdots \\ 0 & -r_n & 1+2r_n & -r_n & \cdots \\ \vdots & \ddots & \ddots & \ddots & \cdots \\ \vdots & \cdots & -r_n & 1+2r_n & -r_n \\ 0 & \cdots & \cdots & \cdots & 1 \end{bmatrix} \begin{pmatrix} \Theta_{l,1}^{n+1} \\ \Theta_{l,2}^{n+1} \\ \Theta_{l,3}^{n+1} \\ \vdots \\ \Theta_{l,i}^{n+1} \\ \Theta_{l,i+1}^{n+1} \end{pmatrix} = \begin{pmatrix} 0 \\ \Theta_{l,2}^{n} \\ \Theta_{l,3}^{n} \\ \vdots \\ \Theta_{l,i}^{n} \\ 0 \end{pmatrix} + \begin{pmatrix} \Theta_d \\ 0 \\ 0 \\ \vdots \\ 0 \\ 1 \end{pmatrix} \tag{37}$$

in the developed form including boundary conditions In the solid phase, we have $BJ^{n+1} = J^n + D$ corresponding to

$$\begin{bmatrix} 1 & 0 & \cdots & \cdots & 0 & \\ -ar_n & 1+2ar_n & -ar_n & 0 & \cdots & \\ 0 & -ar_n & 1+2ar_n & -ar_n & \cdots & \\ \vdots & \ddots & \ddots & \ddots & \cdots & \\ \vdots & \cdots & -ar_n & 1+2ar_n & -ar_n & \\ 0 & \cdots & \cdots & & \cdots & 1 \end{bmatrix} \begin{pmatrix} \Theta_{s,i+1}^{n+1} \\ \Theta_{s,i+2}^{n+1} \\ \Theta_{s,i+3}^{n+1} \\ \vdots \\ \Theta_{s,N}^{n+1} \\ \Theta_{s,N+1}^{n+1} \end{pmatrix} = \begin{pmatrix} 0 \\ \Theta_{s,i+2}^{n} \\ \Theta_{s,i+3}^{n} \\ \vdots \\ \Theta_{s,N}^{n} \\ 0 \end{pmatrix} + \begin{pmatrix} 1 \\ 0 \\ 0 \\ \vdots \\ 0 \\ \Theta_u \end{pmatrix} \tag{38}$$

Δt_n and Δt_0 are evaluated considering Eqs. (35) and (36).

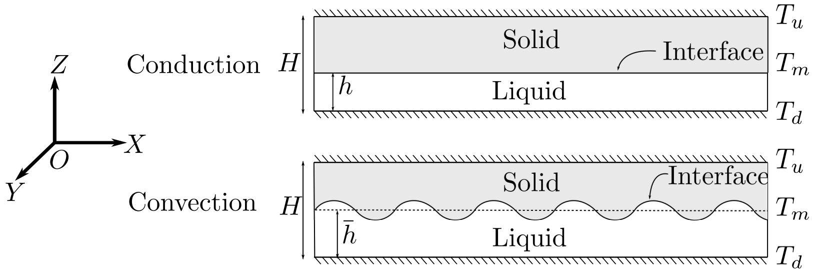

Figure 1: Sketch of a melting solid in conductive regime (above) and convective regime (below)

Properties (phase)	Notation	Measured Values
Melting temperature	T_m	17.5 - 17.9 °C
Enthalpy of melting	ΔH_f	232 kJ kg^{-1}
Enthalpy of solidification	ΔH_s	235 kJ kg^{-1}
Specific heat capacity (solid)	$c_{p,s}$	2.05 kJ kg^{-1} K^{-1}
Specific heat capacity (liquid)	$c_{p,l}$	2.21 kJ kg^{-1} K^{-1}
Thermal conductivity (solid)	Λ_s	0.34 W m^{-1} K^{-1}
Thermal conductivity (liquid)	Λ_l	0.16 W m^{-1} K^{-1}
Density (liquid)	ρ	773.4 kg.m^{-3} at 20 °C
Thermal expansion coefficient (liquid)	α	8.98 10^{-4} °C^{-1}
Viscosity (liquid)	η	3.26 10^{-3}Pa s^{-1} at 20 °C

Table 1: Hexadecane properties

time ($\times 10^4$ s)	$\bar{h}$ (mm)	$A = \dfrac{H-\bar{h}}{\bar{h}}$	Fluid region
0.7-0.8	3.1	6.9	motionless
1.6-1.8	3.9	5.4	onset of convection
2.5-2.7	5.6	3.4	convection
3.5-3.6	6.7	2.7	convection
8.5-8.6	8.5	1.9	convection and steady state

Table 2: Values of the mean liquid height $\bar{h}$ and the ratio of solid to liquid height A along time. Set of experimental parameters: H= 25 mm, $AR = 4.56$ and $\Delta T = 9.6\,°$C.

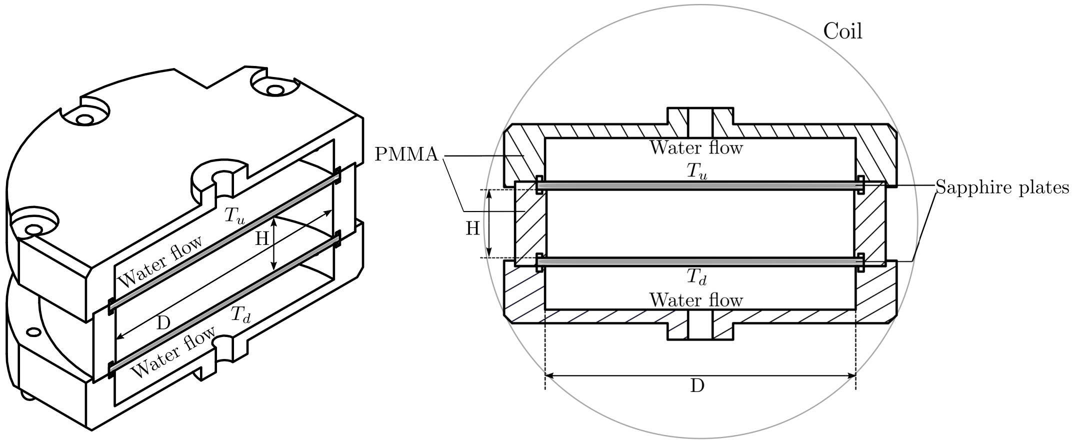

Figure 2: Sketch of the setup - Left side: half of the setup ; Right side: vertical cross section.

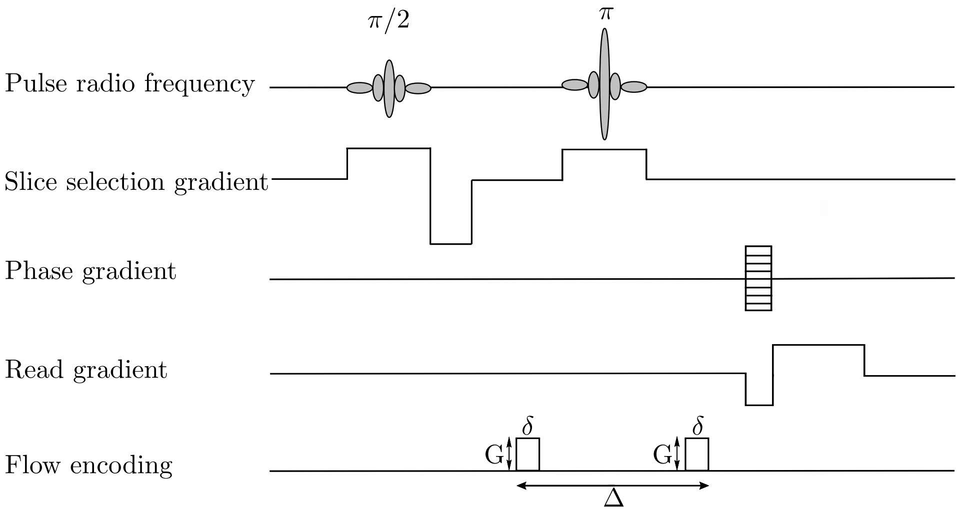

Figure 3: Magnetic Resonance Imaging (MRI) pulse sequence used to obtain velocity map

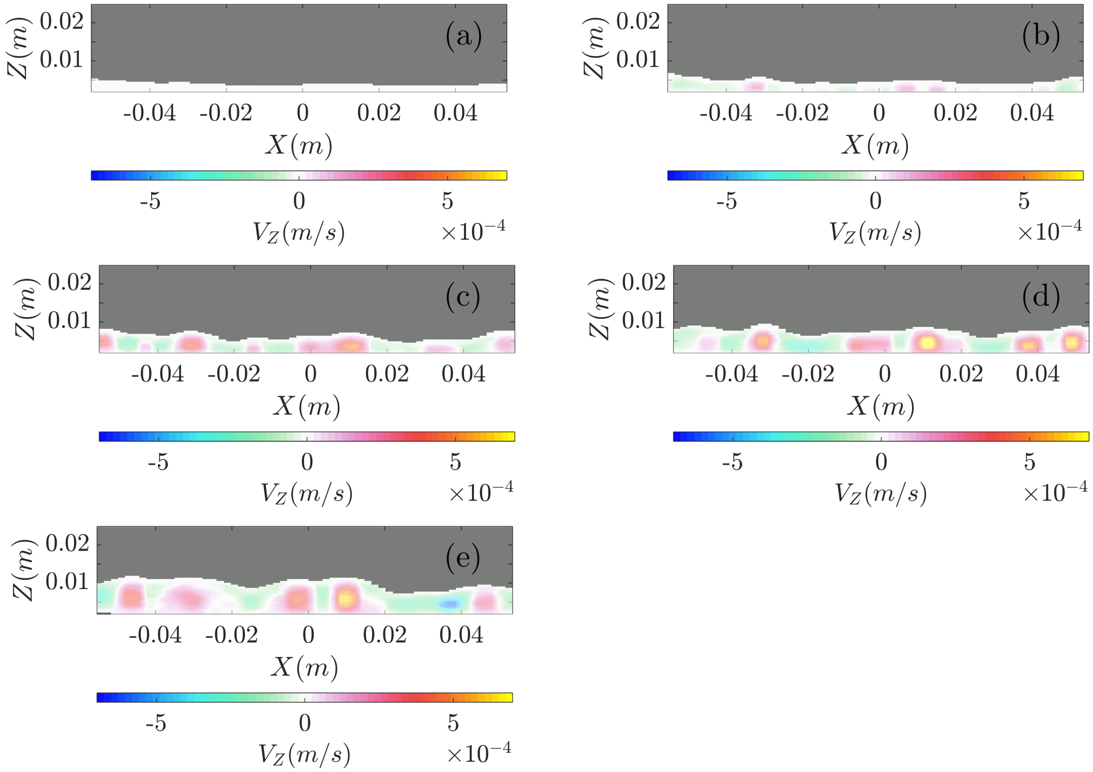

Figure 4: Velocity maps of the vertical component V_z in the liquid phase (Vertical cross-section including the axis of the cylindrical cavity) at different times (a) $t = 0.7 \times 10^4$ s, (b) $t = 1.6 \times 10^4$ s, (c) $t = 2.5 \times 10^4$ s, (d) $t = 3.5 \times 10^4$ s, (e) $t = 8.6 \times 10^4$ s

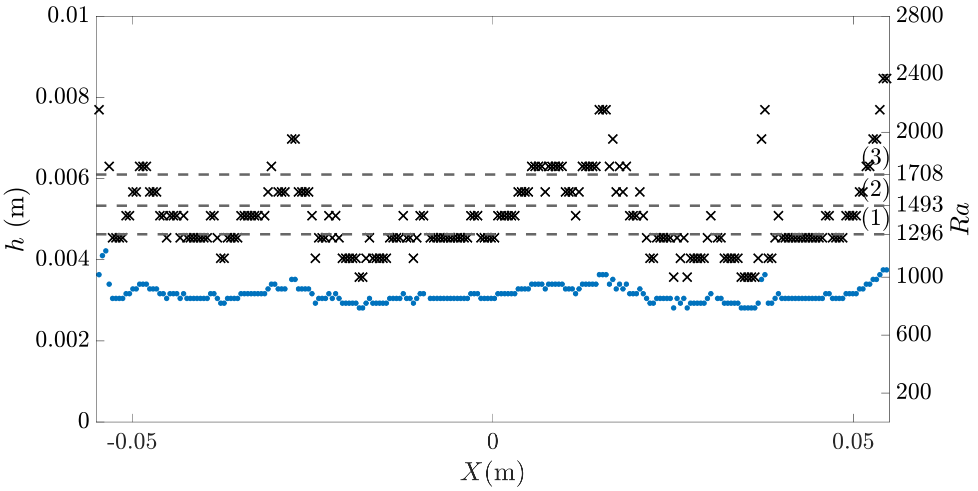

Figure 5: Liquid height h (blue dots) and local Ra (black crosses) corresponding to the onset of convection - RARE experiments. Dotted lines correspond to (1) $Ra = 1296$, (2) $Ra = 1493$ and (3) $Ra = 1708$.

Symbols	Regime	Variation of $\bar{h}$ $\left(A = \dfrac{H-\bar{h}}{\bar{h}}\right)$ over experiments	Total aspect ratio AR
×	Stable conduction	$\bar{h} \nearrow \quad (A \searrow)$	5.9
×	Stable conduction	$\bar{h} \nearrow \quad (A \searrow)$	4.56
●	Unstable conduction	$\bar{h} \nearrow \quad (A \searrow)$	5.9
○	Convection	$\bar{h} \nearrow \quad (A \searrow)$	5.9
◇	Convection	$\bar{h} \searrow \quad (A \nearrow)$	5.9
●	Unstable conduction	$\bar{h} \nearrow \quad (A \searrow)$	4.56
○	Convection	$\bar{h} \nearrow \quad (A \searrow)$	4.56
◇	Convection	$\bar{h} \searrow \quad (A \nearrow)$	4.56

Table 3: Summary of symbols used in Figs. 10-14 regarding experimental conditions.

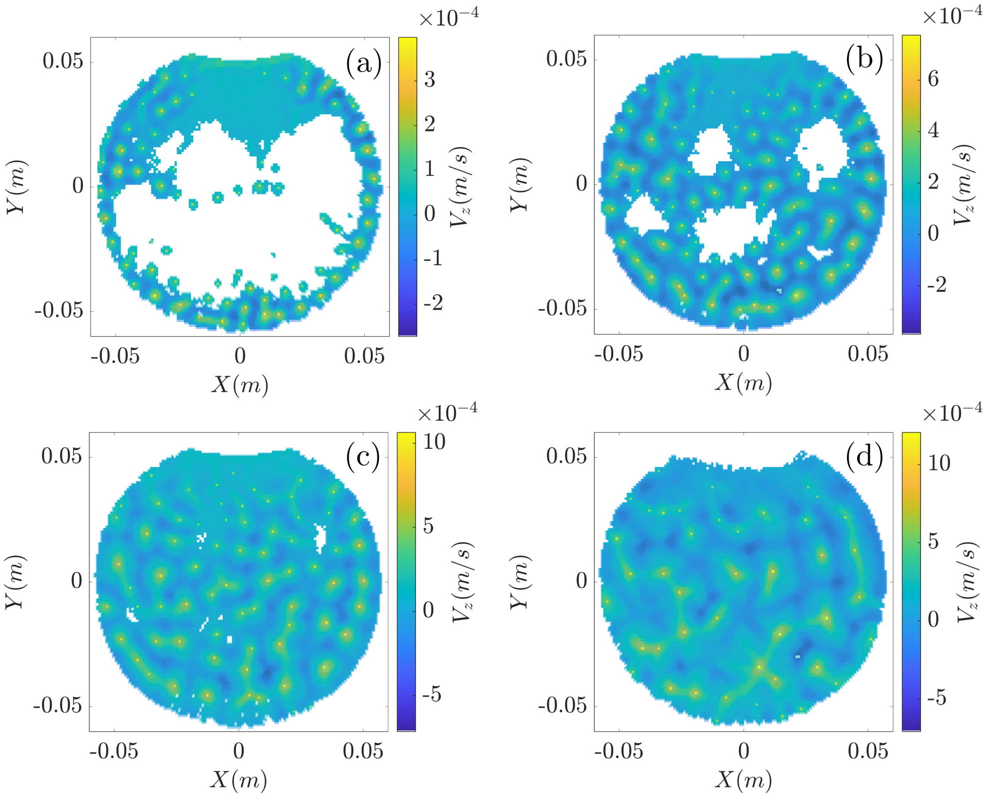

Figure 6: Velocity maps of the vertical component V_z in the liquid phase (horizontal cross-section 4 mm above the lower wall). (a) $t = 1.7 \times 10^4$ s, (b) $t = 2.6 \times 10^4$ s, (c) $t = 3.6 \times 10^4$ s, (d) $t = 8.6 \times 10^4$ s. The white areas correspond to solid phases and yellow dots correspond to the positions of maximal velocity.

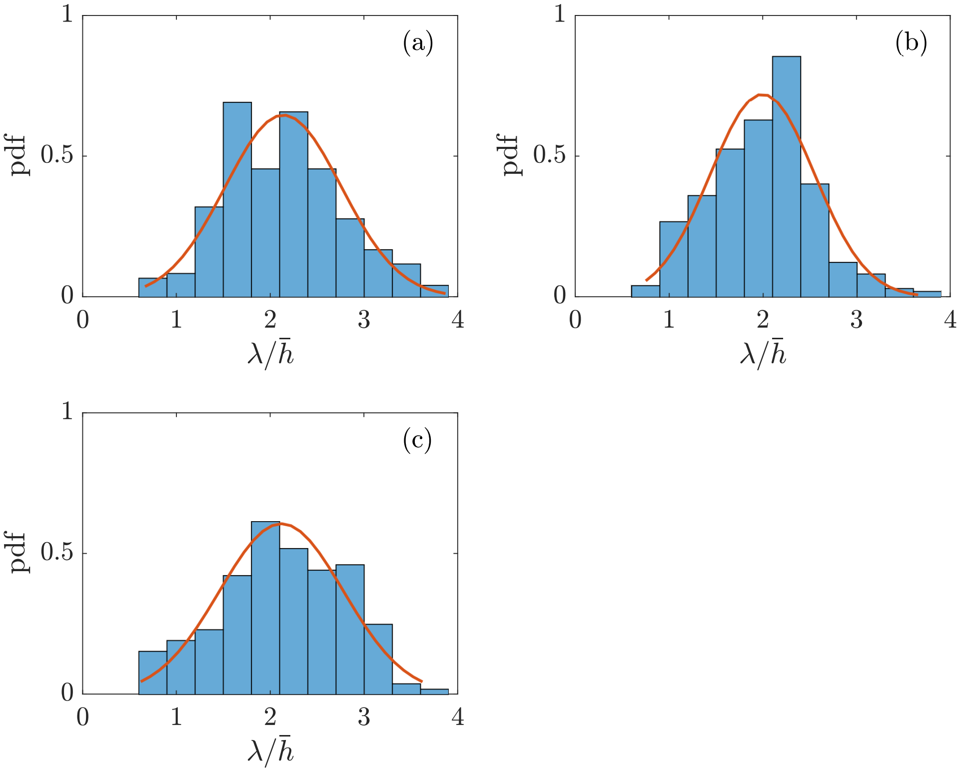

Figure 7: Probability density function (pdf) of the dimensionless wavelengths $\lambda/\bar{h}$. The red line corresponds to the normal distribution $f(\lambda/\bar{h})$ given by Eq. (5) (a) $t = 2.6 \times 10^4$ s (b) $t = 3.6 \times 10^4$ s (c) $t = 8.6 \times 10^4$ s

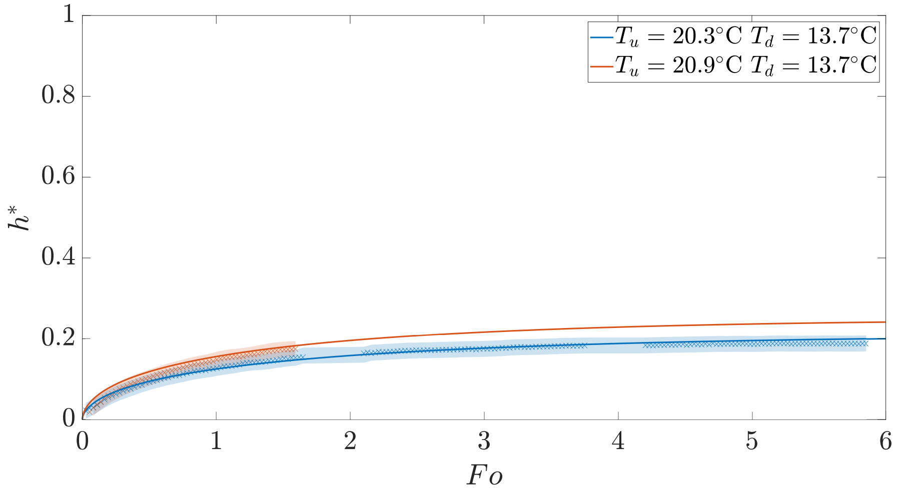

(a) Stable conductive regime

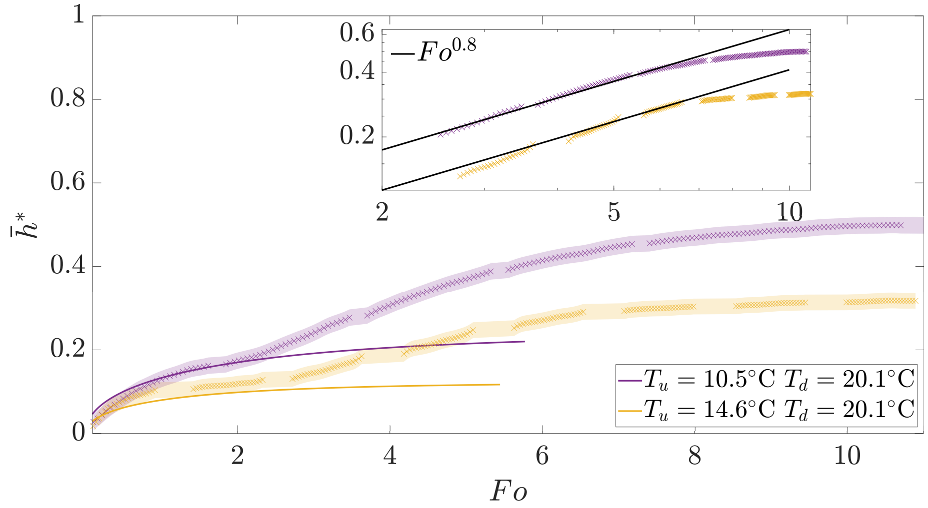

(b) Convective regime

Figure 8: Mean liquid height $\bar{h}^*$ as a function of the Fourier number Fo (a) in stable conductive configurations ($\Delta T < 0$), (b) in unstable configurations ($\Delta T > 0$). Colored continuous lines correspond to the theoretical evolution of $\bar{h}^*$ whose scaling law is $\bar{h}^* \propto \; Fo^{0.5}$ (conductive regime). Deviations from this law correspond to the onset of convection for which $\bar{h}^* \propto Fo^{\frac{1}{2-3\beta}}$ with $\beta = 1/4$.

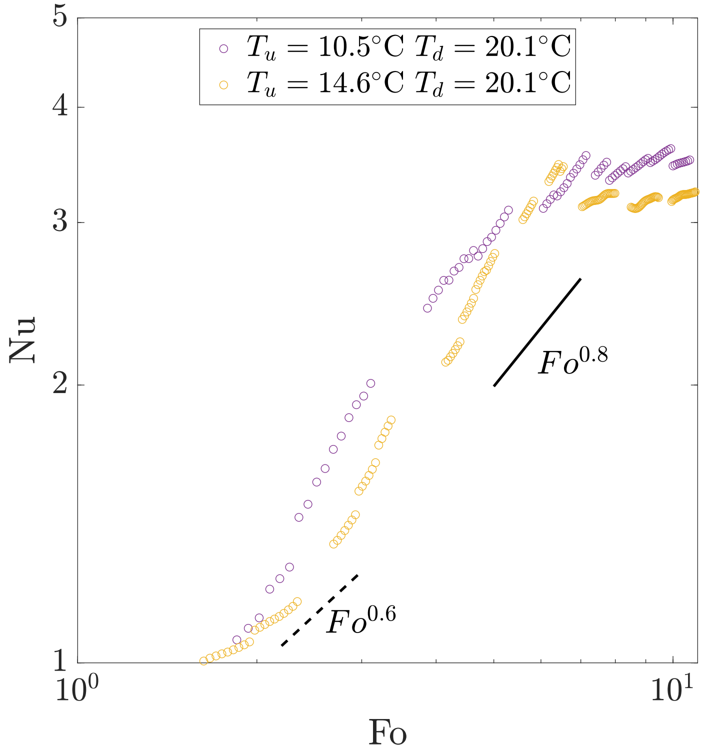

Figure 9: Nusselt number as a function of the Fourier number Fo at the onset of convection

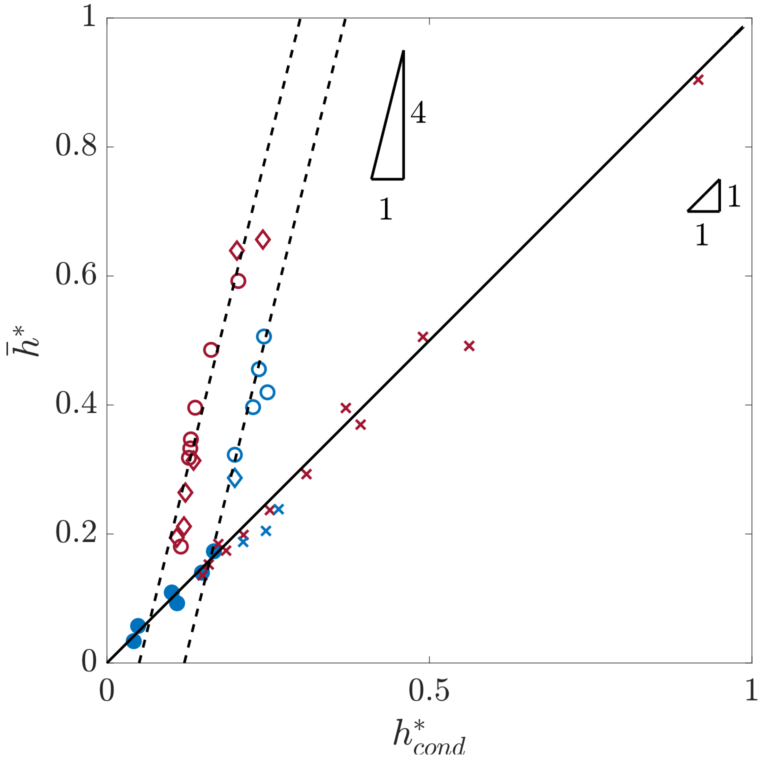

Figure 10: Variations of the experimental dimensionless mean liquid height $\bar{h}/H$ as a function of the theoretical value obtained in conductive regime (Eq. 12). Red symbols: $AR = 4.56$, blue symbols: $AR = 5.9$; Crosses: stable conduction ; Full circles: unstable conduction, Empty circles (resp. diamonds): convective regime obtained for decreasing (resp. increasing) values of A. The legend is also summarized in table 3.

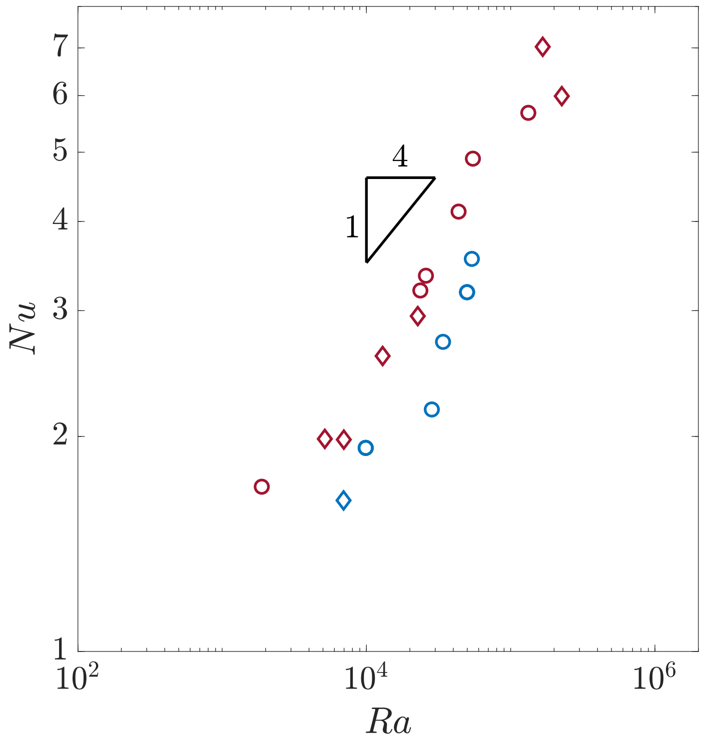

Figure 11: Nusselt number as a function of Rayleigh number in cases $\Delta T > 0$ (Red symbols: $AR = 4.56$ and Blue symbols: $AR = 5.9$). Empty circles (resp. diamonds): convective regime obtained for decreasing (resp. increasing) values of A. The legend is also summarized in table 3.

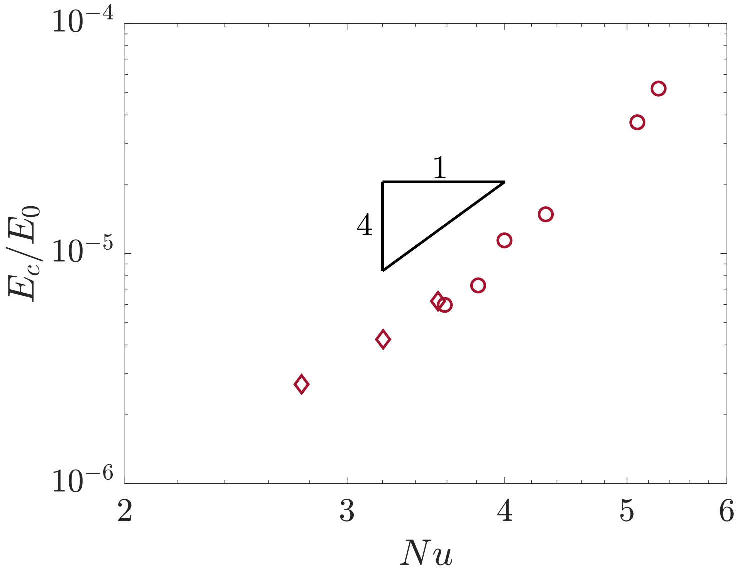

Figure 12: Dimensionless kinetic energy E_c/E_0 as function of the Nusselt number Nu - Convective regime (Red symbols: $AR = 4.56$. Empty circles (resp. diamonds): decreasing (resp. increasing) values of A. The legend is also summarized in table 3.

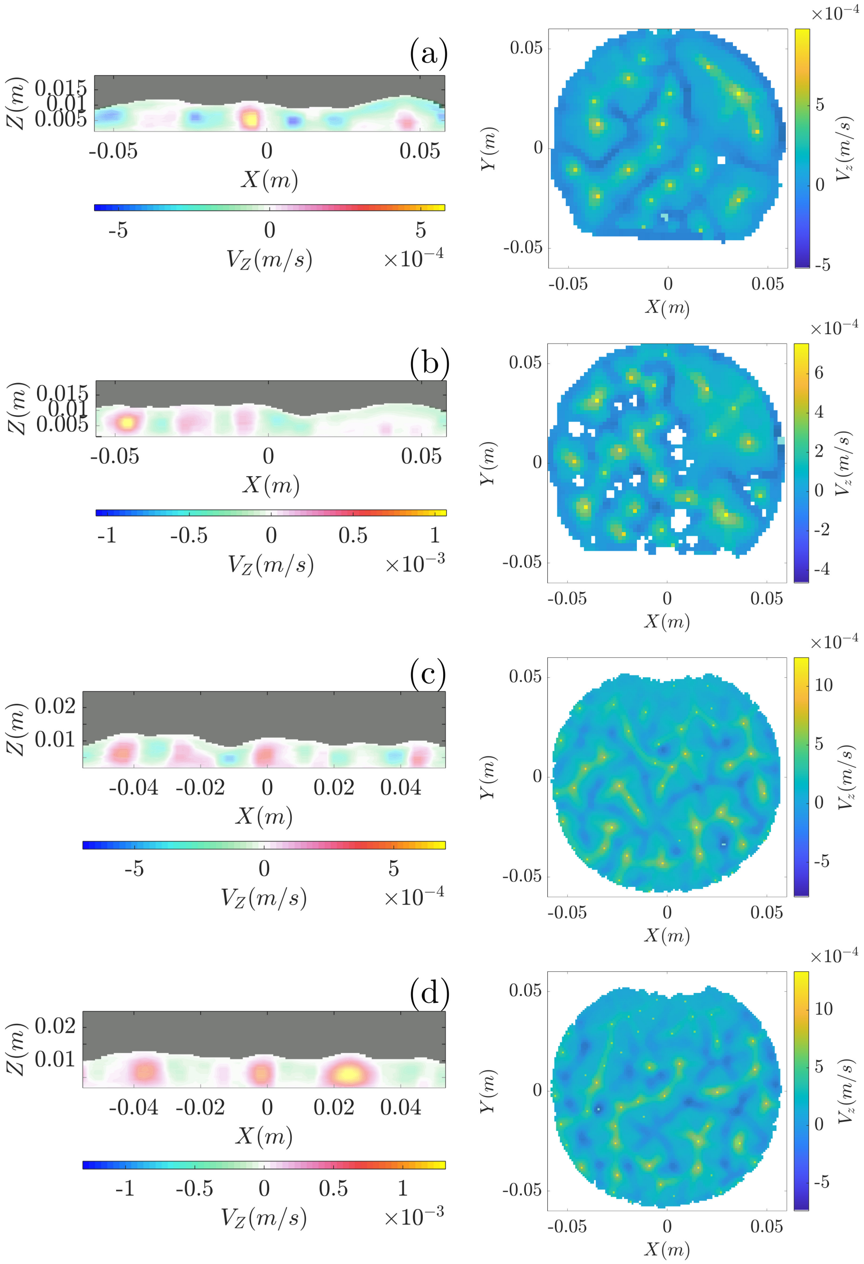

Figure 13: Vertical velocity component in the vertical (X, Z) plane (left) and in a horizontal one in the liquid phase (right) (the horizontal plane is located 10 mm above the lower wall for (a) and (b), 4 mm above the lower wall for (c) and (d)).
Experimental conditions: (a) $H = 0.02$ m, $A = 0.9$, $D/\bar{h} = 11.4$, $Nu = 3.6$ (b) $H = 0.02$ m, $A = 0.9$, $D/\bar{h} = 11.0$, $Nu = 3.5$ (c) $H = 0.025$ m, $A = 2.7$, $D/\bar{h} = 12.6$, $Nu = 3.8$ (d) $H = 0.025$ m, $A = 1.9$, $D/\bar{h} = 11.2$, $Nu = 4.2$

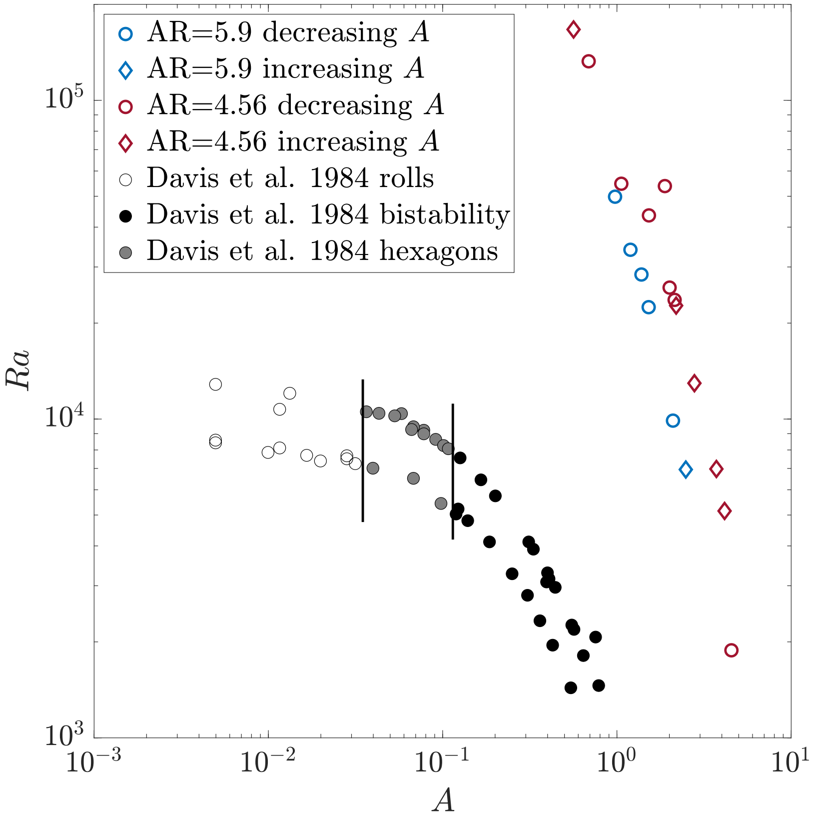

Figure 14: Experimental results summarized in the (Ra, A) diagram.

References

[1] M. G. Worster and GK. Batchelor. Solidification of fluids. *Perspectives in Fluid Dynamics (ed. GK Batchelor, HK Moffatt & MG Worster)*, pages 393–446, 2000.

[2] Q. Schiermeier. Ice loss shifts arctic cycles. *Nature News*, 489(7415):185, 2012.

[3] H. Eicken, TC. Grenfell, DK. Perovich, JA. Richter-Menge, and K. Frey. Hydraulic controls of summer arctic pack ice albedo. *Journal of Geophysical Research: Oceans*, 109(C8), 2004.

[4] H. Eicken. Arctic sea ice needs better forecasts. *Nature*, 497(7450):431–433, 2013.

[5] H. Bénard. Les tourbillons cellulaires dans une nappe liquide. *Rev. Gen. Sci. Pures Appl.*, 11:1261–1271, 1900.

[6] L. Rayleigh. Lix. on convection currents in a horizontal layer of fluid, when the higher temperature is on the under side. *The London, Edinburgh, and Dublin Philosophical Magazine and Journal of Science*, 32(192):529–546, 1916.

[7] EL. Koschmieder. Bénard convection. *Adv. Chem. Phys*, 26:177, 1974.

[8] S. Chandrasekhar. *Hydrodynamic and hydromagnetic stability.* Courier Corporation, 2013.

[9] E. Bodenschatz, W. Pesch, and G. Ahlers. Recent developments in rayleigh-bénard convection. *Annual review of fluid mechanics*, 32(1):709–778, 2000.

[10] F. H. Busse and G. Schubert. Convection in a fluid with two phases. *Journal of Fluid Mechanics*, 46(4):801–812, 1971.

[11] S. H. Davis, U. Müller, and C. Dietsche. Pattern selection in single-component systems coupling Bénard convection and solidification. *Journal of Fluid Mechanics*, 144:133–151, 1984.

[12] C. Dietsche and U. Müller. Influence of Bénard convection on solid–liquid interfaces. *Journal of Fluid Mechanics*, 161(-1):249, 1985.

[13] F. H. Busse. The stability of finite amplitude cellular convection and its relation to an extremum principle. *Journal of Fluid Mechanics*, 30(4):625–649, 1967.

[14] G. M. Vasil and M. R. E. Proctor. Dynamic bifurcations and pattern formation in melting-boundary convection. *Journal of Fluid Mechanics*, 686:77–108, 2011.

[15] B. Favier, J. Purseed, and L. Duchemin. Rayleigh-Bénard convection with a melting boundary. *Journal of Fluid Mechanics*, 858:437–473, 2019.

[16] R.E. Kelly and D. Pal. Thermal convection with spatially periodic boundary conditions: resonant wavelength excitation. *Journal of Fluid Mechanics*, 86(3):24, 1978.

[17] P. Roberts, G. Schubert, K. Zhang, X. Liao, and F. H. Busse. Instabilities in a fluid layer with phase changes. *Physics of the Earth and Planetary Interiors*, 165(3-4):147–157, 2007.

[18] S. Madruga and J. Curbelo. Dynamic of plumes and scaling during the melting of a Phase Change Material heated from below. *International Journal of Heat and Mass Transfer*, 126:206–220, 2018.

[19] O. Satbhai, S. Roy, S. Ghosh, S. Chakraborty, and R. Lakkaraju. Comparison of the quasi-steady-state heat transport in phase-change and classical Rayleigh-Bénard convection for a wide range of Stefan number and Rayleigh number. *Physics of Fluids*, 31(9):096605, 2019.

[20] L.-A. Couston, E. W. Hester, B. Favier, J. R. Taylor, P. R. Holland, and A. Jenkins. Topography generation by melting and freezing in a turbulent shear flow. *Journal of Fluid Mechanics*, 911, 2021.

[21] J. Purseed, B. Favier, L. Duchemin, and E. W. Hester. Bistability in Rayleigh-Bénard convection with a melting boundary. *Physical Review Fluids*, 5(2):023501, 2020.

[22] B. R. Esfahani, S. C. Hirata, S. Berti, and E. Calzavarini. Basal melting driven by turbulent thermal convection. *Physical Review Fluids*, 3(5):053501, 2018.

[23] U. Stritih. An experimental study of enhanced heat transfer in rectangular pcm thermal storage. *International Journal of Heat and Mass Transfer*, 47(12-13):2841–2847, 2004.

[24] B. J. Jones, D. Sun, S. Krishnan, and S. V. Garimella. Experimental and numerical study of melting in a cylinder. *International Journal of Heat and Mass Transfer*, 49(15-16):2724–2738, 2006.

[25] N. . Dhaidan and J.M. Khodadadi. Melting and convection of phase change materials in different shape containers: A review. *Renewable and Sustainable Energy Reviews*, 43:449–477, 2015.

[26] X. Sun, Q. Zhang, M. A. Medina, and K. O. Lee. Experimental observations on the heat transfer enhancement caused by natural convection during melting of solid–liquid phase change materials (PCMs). *Applied Energy*, 162:1453–1461, 2016.

[27] S. Madruga, N. Haruki, and A. Horibe. Experimental and numerical study of melting of the phase change material tetracosane. *International Communications in Heat and Mass Transfer*, 98:163–170, 2018.

[28] M. Parsazadeh and X. Duan. Numerical and Experimental Investigation of Phase Change Heat Transfer in the Presence of Rayleigh–Benard Convection. *Journal of Heat Transfer*, 142(6):062401, 2020.

[29] S.J. Gibbs, T.A. Carpenter, and L.D. Hall. Magnetic resonance imaging of thermal convection. *Journal of Magnetic Resonance, Series A*, 105(2):209–214, 1993.

[30] J. Weis, R. Kimmich, and H.P. Müller. Nmr imaging of thermal convection patterns. *Magnetic Resonance Imaging*, 14(3):319–327, 1996.

[31] M. Darbouli, C. Métivier, S. Leclerc, C. Nouar, M. Bouteera, and D. Stemmelen. Natural convection in shear-thinning fluids: Experimental investigations by MRI. *International Journal of Heat and Mass Transfer*, 95:742–754, 2016.

[32] M. E. Skuntz, B. G. Pelkie, S. L. Codd, R. Anderson, and J. D. Seymour. Axial variability of pattern formation in rayleigh-bénard convection: Mri velocimetry in a low aspect ratio cylinder. *International Communications in Heat and Mass Transfer*, 118:104869, 2020.

[33] P. Aussillous, A. J. Sederman, L. F. Gladden, H. E Huppert, and M. G. Worster. Magnetic resonance imaging of structure and convection in solidifying mushy layers. *Journal of Fluid Mechanics*, 552:99, 2006.

[34] S. Leclerc and C. Métivier. MRI temperature and velocity measurements in a fluid layer with heat transfer. *Experiments in Fluids*, 59(2):34, 2018.

[35] C. Vélez, M. Khayet, and J.M. Ortiz de Zárate. Temperature-dependent thermal properties of solid/liquid phase change even-numbered n-alkanes: n-Hexadecane, n-octadecane and n-eicosane. *Applied Energy*, 143:383–394, 2015.

[36] N. Sgreva, J. Noel, C. Métivier, P. Marchal, M. Isaiev, Cheynes A., Y. Jannot, and S. Leclerc. Physical properties of a pure phase change materials - the hexadecane. *in preparation.*

[37] J. Hennig, A. Nauerth, and H. Friedburg. RARE imaging: A fast imaging method for clinical MR. *Magnetic Resonance in Medicine*, 3(6):823–833, 1986.

[38] M. Stiti, A. Labergue, F. Lemoine, S. Leclerc, and D. Stemmelen. Temperature measurement and state determination of supercooled droplets using laser-induced fluorescence. *Experiments in Fluids*, 60(4):69, 2019.

[39] M. N. Özısık. *Heat Conduction.* John Wiley & Sons, 1993.

[40] S. Grossmann and D. Lohse. Scaling in thermal convection: A unifying theory. *Journal of Fluid Mechanics*, 407:27–56, 2000.

[41] R. J. A. M. Stevens, E. P. Van der Poel, S. Grossmann, and D. Lohse. The unifying theory of scaling in thermal convection: The updated prefactors. *Journal of Fluid Mechanics*, 730:295–308, 2013.